NANO LETTERS

Letter

pubs.acs.org/NanoLett

Seebeck and Figure of Merit Enhancement in Nanostructured Antimony Telluride by Antisite Defect Suppression through Sulfur Doping

Rutvik J. Mehta,[†] Yanliang Zhang,[‡] Hong Zhu,[§] David S. Parker,[∥] Matthew Belley,[‡] David J. Singh,[∥] Ramamurthy Ramprasad,[§] Theodorian Borca-Tasciuc,[‡] and Ganpati Ramanath*,[†]

[†]Materials Science and Engineering Department and [‡]Mechanical, Aerospace & Nuclear Engineering Department, Rensselaer Polytechnic Institute, Troy, New York 12180, United States

[§]Chemical, Materials & Biomolecular Engineering Department, University of Connecticut, Storrs, Connecticut 06269, United States

[∥]Materials Science & Technology Division, Oak Ridge National Laboratory, Oak Ridge, Tennessee 37831-6056, United States

Supporting Information

ABSTRACT: Antimony telluride has a low thermoelectric figure of merit (ZT < ~0.3) because of a low Seebeck coefficient α arising from high degenerate hole concentrations generated by antimony antisite defects. Here, we mitigate this key problem by suppressing antisite defect formation using subatomic percent sulfur doping. The resultant 10−25% higher α in bulk nanocrystalline antimony telluride leads to ZT ~ 0.95 at 423 K, which is superior to the best non-nanostructured antimony telluride alloys. Density functional theory calculations indicate that sulfur increases the antisite formation activation energy and presage further improvements leading to ZT ~ 2 through optimized doping. Our findings are promising for designing novel thermoelectric materials for refrigeration, waste heat recovery, and solar thermal applications.

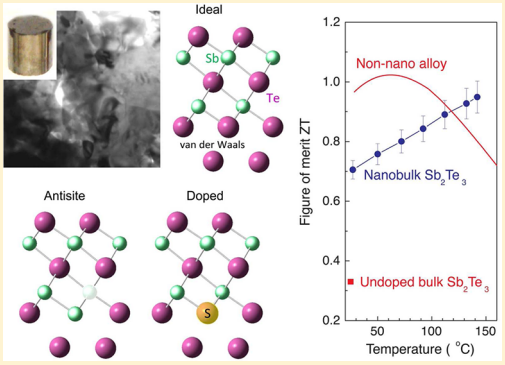

KEYWORDS: *Nanobulk thermoelectrics, sulfur doping, antimony telluride, antisite defects, first principle transport calculations, high figure of merit ZT*

Thermoelectric materials offer promise for realizing transformative solid-state refrigeration technologies that could replace extant ones based on liquid coolants[1] and allow the efficient conversion of waste heat to electricity. The fruition of this vision, however, requires bulk thermoelectric materials with figures of merit ZT > 1 in the $200 \leq T \leq 800$ K range, necessitating high Seebeck coefficient α, high electrical conductivity σ, and low thermal conductivity κ. Pnictogen chalcogenides (V−VI compounds) and their alloys are well-suited for realizing high ZT due to their low band gaps, complex crystal structures, and the presence of heavy elements.[2] Antimony telluride is a p-type semiconductor with σ > 300 $k\Omega^{-1}\cdot m^{-1}$, but the ZT < 0.3 due to low α arising from self-compensating antisite defects.[3−5] In particular, Sb atoms occupying Te sites—denoted as Sb'_{Te}—create acceptor states resulting in high hole concentrations,[6−8] for example, $h > 10^{20}$ cm^{-3}, that in turn leads to low α.

Self-alloying with >10 at. % Te has been shown to yield ZT ~ 0.49 along the [0001] direction[8] of single crystals, but the direction-averaged ZT remained <~0.3. Alloying with ~25 at. % Bi[7−9] not only increases α but also decreases κ due to increased impurity scattering of phonons, leading to the highest room-temperature ZT_{300K} ~ 1 reported for any bulk p-type material. However, such high impurity content decreases the bandgap and precludes the use of this material above 450 K. Lower alloying levels (e.g., <10 at. % of Tl or In)[3,10,11] have been shown to decrease h in single-crystal Sb_2Te_3 but have not resulted in ZT increases. Dopant additions (e.g., <~2 at. %) known to increase ZT in the Pb−Te system[12] have also been of limited utility for controlling the carrier concentration in Sb_2Te_3 due to the self-compensating defect chemistry in this material.

Here, we demonstrate that subatomic-percent sulfur doping of nanostructured Sb_2Te_3 can result in ~25% greater α than the highest reported for the non-nanostructured Sb_2Te_3. We show that sulfur doping increases the Sb'_{Te} antisite defect formation activation energy, thus mitigating the key problem with this material. The resultant hole concentration decrease and possibly an increased valence band density of states near the Fermi level underpin the α enhancement mechanism. The combined effect of sulfur doping and nanostructuring leads to a three times higher ZT than non-nanostructured antimony telluride and holds promise for obtaining ZT ~ 2 by optimized doping. Our findings are of importance for designing high ZT thermoelectric materials

Received: May 1, 2012
Revised: August 7, 2012
Published: August 14, 2012

dx.doi.org/10.1021/nl301639t | *Nano Lett.* 2012, 12, 4523−4529

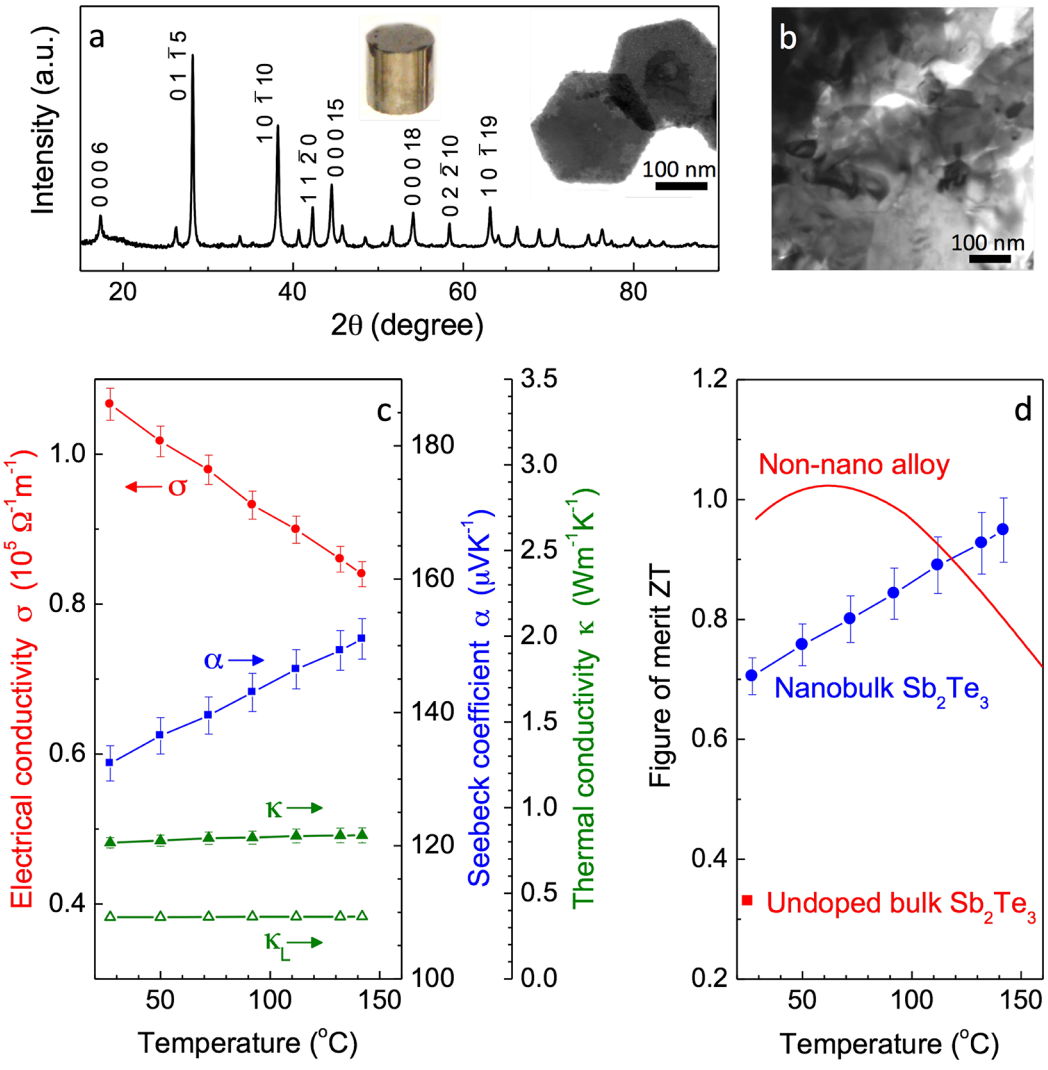

Figure 1. (a) X-ray diffractogram from nanostructured bulk pellets (see photograph inset) fabricated by cold-pressing and sintering S-doped Sb_2Te_3 nanoplates (see TEM inset). Only peaks corresponding to the rhombohedral crystal structure of Sb_2Te_3 are seen; for brevity, only the major peaks are indexed. (b) TEM micrograph showing nanogranular and nanoporous features in the sintered pellets. The thermoelectric properties (c) α, σ, κ, and κ_L and (d) ZT of our nanobulk S-doped Sb_2Te_3 plotted as a function of temperature. Color-coded arrows point to the ordinate to be used for reading the different plots. In d, the ZT values for undoped bulk Sb_2Te_3, and non-nanostructured $Bi_{0.5}Sb_{1.5}Te_3$ alloys (non-nano alloy—data from ref 33) are shown for comparison.

by using a combination of doping and nanostructuring for refrigeration, waste heat recovery, and solar thermal applications.

We synthesized sulfur-doped nanoplates of Sb_2Te_3 by a microwave-stimulated solvothermal approach[13,14] (Figure 1a TEM inset). The nanocrystals were consolidated into nanostructured bulk pellets by cold compaction and sintering (Figure 1a inset and b). X-ray diffractograms of the nanobulk pellets confirm the retention of the rhombohedral $R\bar{3}m$ structure, with no observable traces of extraneous phases (Figure 1a). Energy and wavelength dispersive X-ray spectroscopy (EDX and WDX) confirm 0.1−0.5 at. % sulfur and stoichiometric Sb_2Te_3 with 40 ± 1 at. % Sb and 60 ± 1 at. % Te. The sintered nanobulk pellets have ~92 ± 3% of the theoretical density. We measured κ and α of the nanobulk pellets by a steady state method described in detail elsewhere.[14,15] A four-probe tool in the van der Pauw configuration was used to measure σ. Our measurements of α, σ, and κ along axial and radial directions yielded identical values within instrumental uncertainty, confirming the isotropic properties of our nanobulk Sb_2Te_3. Hole concentrations h and mobility μ were determined from Hall measurements.

We obtain high room-temperature electrical conductivity in the $90 \leq \sigma \leq 150$ $k\Omega^{-1}\cdot m^{-1}$ range (see Figure 1c), comparable to the lower σ ranges reported for single crystal Sb_2Te_3, but hundred- to thousand-fold higher than that of other reports on nanocrystal assemblies.[16,17] Our nanobulk Sb_2Te_3 show $110 \leq \alpha \leq 135$ $\mu V\cdot K^{-1}$, which is more than 50% higher than that of non-nanostructured stoichiometric Sb_2Te_3 and approximately 10−25% higher than the highest α observed for off-stoichiometric non-nanostructured Sb_2Te_3. Our isotropic nanobulk Sb_2Te_3 has ~10% higher α than the highest α in single crystals with similar carrier concentration but lower than that of p-type Sb-rich Sb−Bi−Te alloys.[7,8] Previous reports of nanostructured Sb_2Te_3 with unknown or nondeliberate doping have either not shown increases in α[18] (Figure 2b) or the α increase compromises σ significantly. For example, microwave synthesized nanostructured Sb_2Te_3 with unknown doping chemistry[19,20] reports similar or higher α as exhibited by our S-doped Sb_2Te_3, but the

dx.doi.org/10.1021/nl301639t | Nano Lett. 2012, 12, 4523−4529

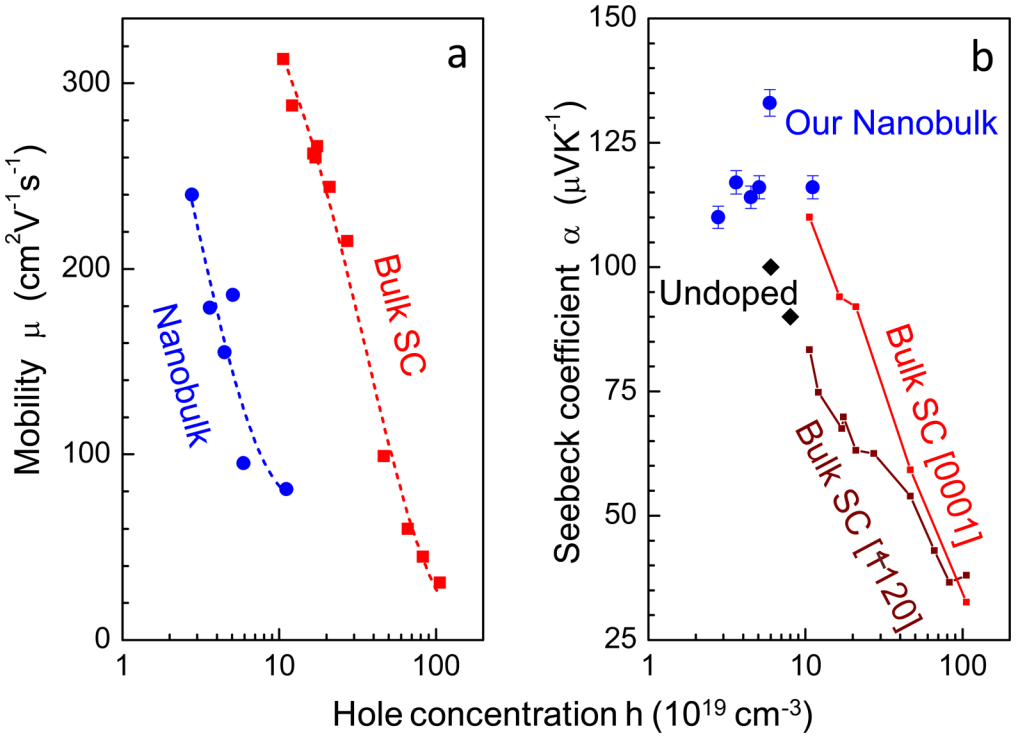

Figure 2. Plots of (a) hole mobility μ and (b) Seebeck coefficient α, as a function of hole concentration h, in our nanobulk S-doped Sb_2Te_3 pellets (blue circles). For comparison, data from ref 8 are shown for undoped bulk single-crystal Sb_2Te_3 (SC) for two crystallographic directions (red and maroon) and from ref 18 for undoped nanostructured Sb_2Te_3 (black diamonds).

σ is more than 10- to 100-fold lower than both conventional non-nanostructured and our doped nanobulk Sb_2Te_3, which translates to at least 2−3 fold lower ZT than ours.

Our nanobulk Sb_2Te_3 exhibit room-temperature thermal conductivity in the $0.7 \leq \kappa \leq 1.1$ $W \cdot m^{-1} \cdot K^{-1}$ range,[14] which is ~40−70% lower than that of the single- or polycrystalline Sb_2Te_3. This κ decrease corresponds to about 60−75% diminution in the lattice thermal conductivity κ_L due to phonon scattering by the ~20−50 nm nanograins[14] and nanopores.[21] The high σ, ultralow κ, and enhanced α in nanobulk Sb_2Te_3 yield $ZT_{300K} \sim 0.75$, which is more than 2- to 4-fold that of non-nanostructured poly- or single-crystalline antimony telluride[7,8] (Figure 1d).

The ZT of our nanobulk Sb_2Te_3[14] increases monotonically between $300 \leq T \leq 423$ K, reaching $ZT_{423K} = 0.95$, which is ~35% higher than $ZT_{423K} \sim 0.7$ reported for non-nanostructured $Sb_{1.5}Bi_{0.5}Te_3$ alloys.[7,8] This ZT increase is mainly due to the monotonic α increase with temperature, yielding values as high as $\alpha_{423K} \sim 150$ $\mu V \cdot K^{-1}$ (Figure 1c). We expect α to peak at higher temperatures than that of $Sb_{1.5}Bi_{0.5}Te_3$ alloys and Bi_2Te_3, because of the higher temperature onset of bipolar conduction arising from the larger bandgap of Sb_2Te_3. Both σ and κ remain relatively unchanged within ~20% in the $300 \leq T \leq 423$ K range (see Figure 1c). The weaker-than-typical temperature dependence of σ, reminiscent of degenerate doping implies significant scattering due to grain boundaries and/or point defects, leaving open the scope for further ZT improvements by optimizing grain size and/or defect concentrations. The insensitivity of κ is expected above the Debye temperature Θ_D (~160 K for antimony telluride[22]) for nanostructured materials.[14] These effects combined with the higher α endow our nanobulk Sb_2Te_3 with high ZT *without* alloying.

Room-temperature Hall measurements on the nanobulk pellets reveal hole concentrations of $10^{19} \leq h \leq 10^{20}$ cm^{-3} that are about 10- to 100-fold smaller than that reported for both polycrystalline and single-crystal non-nanostructured Sb_2Te_3.[7,8] The hole mobilities of $75 \leq \mu \leq 250$ $cm^2 \cdot V^{-1} \cdot s^{-1}$ are lower than that of single crystals as expected, but higher than non-nanostructured Sb-rich Sb−Bi−Te alloys[7,8] (Figure 2a) probably because the low <1 at. % sulfur doping levels diminish impurity scattering of holes. This behavior is in contrast to dopants such as Bi, Tl and In that are known to degrade μ at even low concentrations.[7,23] The low decrease in μ thus offsets decreases in h to maintain a high σ in our nanobulk Sb_2Te_3. The α is isotropic and varies rather weakly with h in the measured range of $3 \times 10^{19} \leq h \leq 10^{20}$ cm^{-3}, contrary to the strong α−h dependence expected (see Figure 2b). Isotropic α is consistent with the lack of crystallographic texture[14] but unlike anisotropic α seen in single-crystal Sb_2Te_3 due to holes from two bands.[24] The weak dependence of α on h, contrary to the more usual variation found in the theoretical result, may be due to spatial inhomogeneities in stoichiometry and sulfur doping giving rise to regions of varying carrier concentration,[25] considering the lack of second phase within the detection limit of our X-ray diffraction experiments. In general, the nanoscale regions of highest σ will preferentially determine the measured α, provided such regions exceed the percolation threshold. This suggests optimizing the spatial distribution of dopants could further improve α.

The 10−25% increase in α can be traced to the effect of sulfur doping on the antisite defect chemistry in Sb_2Te_3. The similar electronegativities of Sb and Te facilitates Sb'_{Te} antisite defect formation. Each Sb'_{Te} generates a hole by the reaction

$$2Sb_{Sb} + 3Te_{Te} \leftrightarrow 2Sb'_{Te} + 2h + V^{\bullet\bullet}_{Te} + 2V''_{Sb} + 3/2Te_2(g)$$

dx.doi.org/10.1021/nl301639t | *Nano Lett.* 2012, 12, 4523−4529

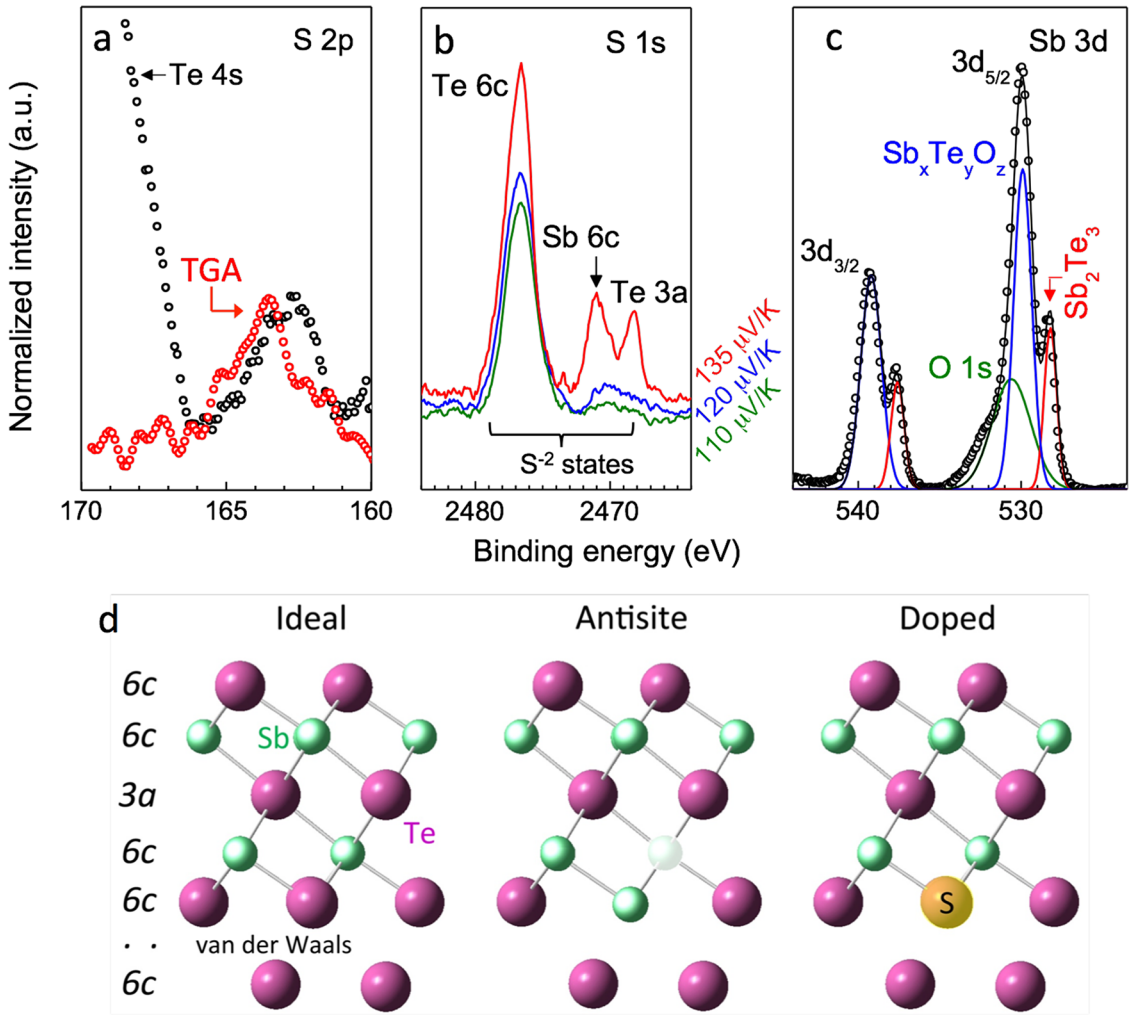

Figure 3. (a) Core-level S 2p band structure obtained by XPS from as-synthesized Sb_2Te_3 nanoplate powders. A baseline spectrum from neat TGA is shown for reference. (b) Core-level S 1s band structure obtained by synchrotron XPS from sintered nanostructured bulk pellets of S-doped Sb_2Te_3 with different α values, shown alongside the spectra. The sub-bands are labeled with Wyckoff sites that specify sulfur occupancy; see text for details. (c) Core-level Sb 3d band structure with sub-bands from unoxidized and oxidized Sb_2Te_3 and the overlapping O 1s indicated. (d) Schematic atomic structures of Sb_2Te_3 with Wyckoff site labels depicting mixed ionic-covalent bonded quintet layers held by interlayer van der Waals bonding in the undoped, defect-free configuration (left), with an antisite Sb'_{Te} defect (center), and with sulfur doping (right). The Wyckoff site notations are indicated on the left. We used supercells of these structures for our DFT calculations.

where $V^{\bullet\bullet}_{Te}$ and V''_{Sb} are vacancies.[3,4,26] The consequent high hole concentrations decrease α. We propose that doping with sulfur, which has a higher electronegativity than Te, decreases h by suppressing Sb'_{Te} formation, thereby offering a means for increasing α. This hypothesis is supported by the sulfur core-level band structure of the nanoplates and the nanobulk pellets measured by X-ray photoelectron spectroscopy (XPS) as described below.

The S 2p band at 162 eV indicates thioligation of Sb_2Te_3 nanoplate surfaces with thioglycolic acid (TGA) used in our synthesis;[14,27] unfettered TGA has a higher binding energy peak at 164 eV (Figure 3a). Synchrotron XPS of the nanobulk pellets reveals three S 1s sub-bands at 2477, 2471, and 2468 eV whose intensities scale with the sulfur doping level measured by WDX (Figure 3b). All three sub-bands correspond to S^{2-} states (higher oxidation numbers are expected[28] only above 2480 eV) and can be identified with sulfur occupancy of specific sites based on the inverse correlation between valence electron density and core-level binding energy. Sulfur at the Te 3*a* site, bound to two layers of electropositive Sb (see Figure 3d), would have the highest electron density and the lowest core-level binding energy. Sulfur at the Sb 6*c* site bound to two layers of isovalent Te would have a higher binding energy. Sulfur at the Te 6*c* site would have the highest binding energy because of a heterocovalent bond with one layer of Sb and weakly bound to Te atoms in the adjacent layer of the $R\bar{3}m$ structure via van der Waals bonding.

We note that only the Te 6*c* sub-band intensity of S 1s strongly correlates with increasing α (Figure 3b), suggesting that this state exerts the largest influence on the hole concentration. The Te 3*a* and Sb 6*c* sites appear to be filled only after the Te 6*c* sites are first filled to a threshold concentration. Such hierarchical site occupancy reported in selenium-alloyed bismuth telluride[8] may be associated with the ease of interlayer sulfur incorporation in the $R\bar{3}m$ structure and lattice strain effects. Considering x moles of sulfur and y moles of decrease in Sb'_{Te}, and hence h, per mole of Sb_2Te_3 at equilibrium, we can write

dx.doi.org/10.1021/nl301639t | *Nano Lett.* 2012, 12, 4523–4529

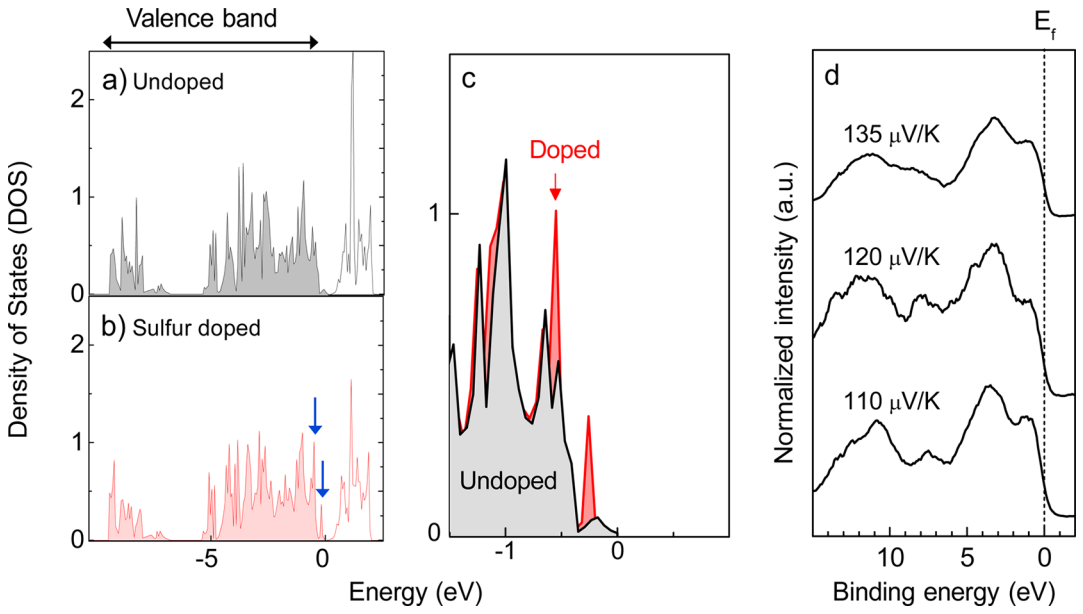

Figure 4. Density of states computed using DFT calculations for (a) undoped and (b) sulfur-doped Sb_2Te_3. The energy scale is referred to the valence band maximum and E_F, arbitrarily set to zero, connotes the Fermi level. Sulfur doping increases the density of states in the valence band as can be clearly seen in (c) a magnified view of superimposed density of states of undoped (gray) and S-doped (red). (d) Valence band spectra obtained by synchrotron XPS from our nanobulk S-doped Sb_2Te_3 pellets.

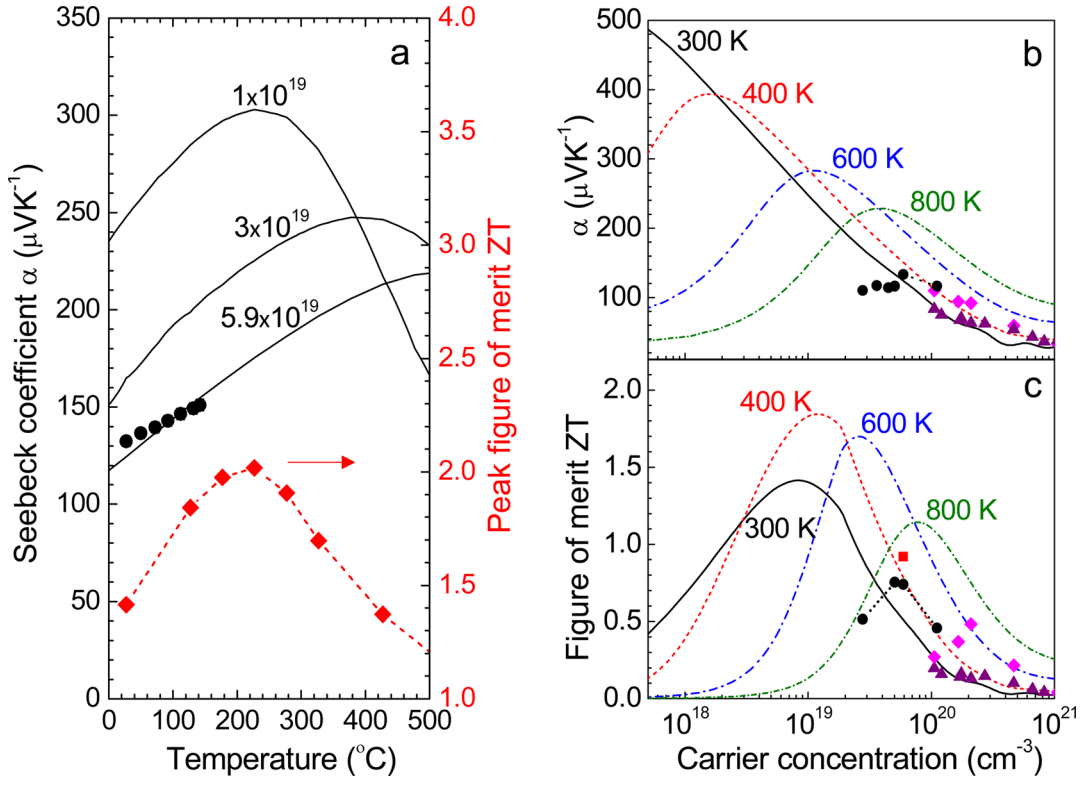

Figure 5. (a) Planar [11$\bar{2}$0] Seebeck coefficient α for three different carrier concentrations (in cm^{-3}), and peak ZT, calculated as a function of temperature. The black circles represent experimentally measured α in our isotropic nanobulk. (b) Pisarenko plot of the planar [11$\bar{2}$0] α and (c) estimated ZT of nanobulk Sb_2Te_3, both calculated by DFT as a function of hole concentration for various temperatures. Experimental data from sulfur-doped nanobulk Sb_2Te_3 at 300 K (black circles) and 400 K (red square) are also shown for comparison, along with 300 K data for bulk single-crystal Sb_2Te_3 from ref 8 for two crystallographic directions [0001] (magenta diamonds) and planar [11$\bar{2}$0] (purple triangles).

dx.doi.org/10.1021/nl301639t | *Nano Lett.* 2012, 12, 4523−4529

$$xS + 2Sb_{Sb} + 3Te_{Te} \Leftrightarrow ySb_{Sb}^{\times} + xS_{Te}^{\times} + (2-y)Sb'_{Te} + (2-y)h + (1+x-y)V_{Te}^{\bullet\bullet} + (2-y)V_{Sb}''' + 3/2Te_2(g)$$

Although we expect $x = y$, our experimental result shows that the h decrease exceeds sulfur doping by 15−20%; that is, $y > x$. We attribute this greater-than-anticipated effectiveness of sulfur doping to a higher activation energy[3,10,29] for creating Sb'_{Te} defects in sulfur-doped Sb_2Te_3, than its undoped counterpart. The increase in activation energy for Sb'_{Te} formation ΔE_S due to sulfur doping can be estimated by recognizing that

$$[Sb'_{Te}] \propto (c_{Sb} - c_S)\exp - [(E_0 + \Delta E_s)/(kT_m)]$$

where c_{Sb} and c_S are Sb and S concentrations, respectively, T_m the melting point, and E_0 the activation energy[3,10,29] in undoped Sb_2Te_3. Setting $[Sb'_{Te}] = h$ from Hall measurements of nanobulk pellets with different c_{Sb} and c_S quantified by WDX, we obtain $\Delta E_S \sim 0.06$ eV connoting a 17% increase over $E_0 \sim 0.35$ eV. This result is corroborated by density functional theory (DFT) calculations showing $\Delta E_S \sim 0.05$ eV for uncharged Sb'_{Te} at the Te 6*c* site (see Figure 3d). Calculations with singly charged antisite defects result in $\Delta E_S \sim 0.17$ eV, suggesting that the antisite defects are predominantly uncharged. This result is also consistent with all of the Sb $3d^{5/2}$ core-level bands being attributable to Sb−Te bonds[14] (Figure 3c) and residual surface oxide and the lack of charged state signatures expected at >530 eV. We are thus persuaded to conclude that subatomic percent doping of substitutional sulfur—supposed to be electronically inactive in pnictogen chalcogenides[26]—is more effective in tuning carrier concentration than adding tens of atomic percent of alloying elements[11,23,29] which degrade the charge carrier mobility.

Our DFT supercell calculations also reveal that sulfur doping increases the density of states close to the valence band maximum (Figures 4a−c) and creates an additional peak in the 1−2.5 at. % doping range. This result suggests the possibility of resonant states[30] that can lead to increased α, although this could also be due to limitations of the supercell approximation. The valence band spectra obtained by synchrotron XPS[31] (see Figure 4d) agree with envelope profiles of the discrete structure obtained by the DFT calculations, but no resonant states are discernible (see Figure 4d). The absence of an O 2p peak at ∼5 eV in the valence band points to inhibited oxidation[32] and absence of oxygen doping. The above results confirm sulfur doping is responsible for the observed α increase, but the question of whether or not there are resonant states remains open.

The high ZT ∼ 0.95 at 420 K despite a comparatively low $\alpha \sim 150\ \mu V \cdot K^{-1}$ suggests the possibility of accessing even higher ZT through optimized doping. To estimate optimal doping, results of first principles band structure calculations carried out using the linearized augmented plane wave method (see Supporting Information) were used to determine α as a function of doping and temperature based on Boltzmann transport theory. Our calculations indicate a substantial increase in α at $h < 10^{19}$ cm^{-3} for a wide temperature range of $300 \leq T \leq 800$ K (Figures 5a,b) with α maxima $\geq 200\ \mu V \cdot K^{-1}$, without entering the bipolar regime at 300 K. The theoretical calculations agree well with experimentally determined α in the 300−450 K range (Figure 5a,b), confirming the applicability of our approach.

We calculated ZT as a function of temperature and hole concentration from experimentally measured κ_L, and μ as function of h, and theoretically determined α, Lorenz number and κ_e using first principles transport calculations. We find $1.7 \leq$ peak ZT ≤ 2 for $400 \leq T \leq 600$ K for $h < 3 \times 10^{19}$ cm^{-3} (Figure 5b,c). For example, peak ZT ∼ 2 at 500 K for $h \sim 1.4 \times 10^{19}$ cm^{-3} and decreases to 1.2 at 800 K due to bipolar conduction. For nanobulk Sb_2Te_3 with higher h, the ZT peaks at higher temperatures, and for a factor of 10 increase in h the peak ZT shifts from 300 to 800 K. These results predict unprecedented ZT ∼ 2 without alloying if the antisite defects can be suppressed further by optimal sulfur doping. Furthermore, as mentioned earlier, the weak temperature-dependence of σ suggests that the power factor $\alpha^2\sigma$ and ZT can be improved further via optimization of the grain size and nanostructure.

In summary, we have demonstrated a novel approach for producing high ZT thermoelectrics by the use of subatomic percent sulfur doping. Sulfur substitution of isovalent Te 6*c* sites suppresses antisite defect formation. The resultant 10- to 100-fold decrease in the hole concentration increases α by 10−25% over the highest observed in nondoped counterparts. Subatomic sulfur doping also fosters high σ due to the diminished effect of impurity scattering of holes, while nanostructuring results in ultralow κ. Cumulatively, we obtain 3-fold higher ZT∼0.95 than non-nanostructured analogues at 423 K and the state-of-art alloys. Our experimental results and theoretical predictions presage that further gains in α, and hence ZT, are possible by manipulating dopant type, level, and site occupancy. Our approach of doping-induced α increase and nanostructuring-induced κ diminution, without compromising σ, opens up new opportunities for obtaining ZT > 2 and transforming thermoelectric refrigeration and energy-harvesting.

■ ASSOCIATED CONTENT

Ⓢ Supporting Information

Experimental methods and materials: nanoplate synthesis, nanobulk fabrication, materials characterization, thermoelectric transport characterization, and theoretical modeling as well as a Pisarenko and Weidemann Franz plots (Figure S1). This material is available free of charge via the Internet at http://pubs.acs.org.

■ AUTHOR INFORMATION

Corresponding Author

*E-mail: Ramanath@rpi.edu.

Notes

The authors declare no competing financial interest.

■ ACKNOWLEDGMENTS

We gratefully acknowledge funding from the U.S. Department of Energy through the S^{3}TEC Energy Frontier Research Center (G.R. and T.B.T.), and partial support from National Science Foundation grant ECCS 1002282/301 (R.R. and G.R.), and the Kaiteki Institute, Japan (G.R. and T.B.T.). We thank Dr. Joe Woicik, Dr. Barry Karlin, and Dr. Dan Fischer for help with setting up the photoemission experiments carried out at the National Synchrotron Light Source at Brookhaven National Laboratory, supported under the U.S. Department of Energy Contract DE-AC02-98CH10886.

■ REFERENCES

(1) Minnich, A. J.; Dresselhaus, M. S.; Ren, Z. F.; Chen, G. *Energy Environ. Sci.* **2009**, *2*, 466−479.

(2) Nolas, G. S.; Sharp, J.; Goldsmid, H. J. *Thermoelectrics: Basic principles and new materials developments*; Springer: New York, 2001.

(3) Horak, J.; Koudelka, L.; Klikorka, J. *React. Solids* **1988**, *5*, 351−359.
(4) Horak, J.; Drasar, C.; Novotny, R.; Karamazov, S.; Lostak, P. *Phys. Status Solidi A* **1995**, *149*, 549−556.
(5) Drasar, C.; Lostak, P.; Uher, C. *J. Electron. Mater.* **2010**, *39*, 2162−2164.
(6) Zhitinskaya, M. K.; Nemov, S. A.; Ivanova, L. D. *Phys. Solid State* **2002**, *44*, 42−47.
(7) Rowe, D. M. *Thermoelectrics Handbook: Macro to Nano*; CRC Press: Boca Raton, FL, 2005.
(8) Rowe, D. M. *CRC Handbook of Thermoelectrics*; CRC Press: Boca Raton, FL, 1995.
(9) Stary, Z.; Horak, J.; Stordeur, M.; Stolzer, M. *J. Phys. Chem. Solids* **1988**, *49*, 29−34.
(10) Lostak, P.; Karamazov, S.; Horak, J. *Phys. Status Solidi A* **1994**, *143*, 271−276.
(11) Horak, J.; Stary, Z.; Lostak, P.; Pancir, J. *J. Phys. Chem. Solids* **1988**, *49*, 191−198.
(12) Kanatzidis, M. G. *Chem. Mater.* **2010**, *22*, 648−659.
(13) Mehta, R. J.; Karthik, C.; Singh, B.; Teki, R.; Borca-Tasciuc, T.; Ramanath, G. *ACS Nano* **2010**, *4*, 5055−5060.
(14) Mehta, R. J.; Zhang, Y. L.; Karthik, C.; Singh, B.; Siegel, R. W.; Borca-Tasciuc, T.; Ramanath, G. *Nat. Mater.* **2012**, *11*, 233−240.
(15) Pal, S. K.; Son, Y.; Borca-Tasciuc, T.; Borca-Tasciuc, D. A.; Kar, S.; Vajtai, R.; Ajayan, P. A. *J. Mater. Res.* **2008**, *23*, 2099−2105.
(16) Zhao, Y. X.; Dyck, J. S.; Hernandez, B. M.; Burda, C. *J. Am. Chem. Soc.* **2010**, *132*, 4982−4983.
(17) Scheele, M.; Oeschler, N.; Veremchuk, I.; Reinsberg, K. G.; Kreuziger, A. M.; Kornowski, A.; Broekaert, J.; Klinke, C.; Weller, H. *ACS Nano* **2010**, *4*, 4283−4291.
(18) Pelz, U.; Kaspar, K.; Schmidt, S.; Dold, M.; Jagle, M.; Pfaadt, A.; Hillebrecht, H. *J. Electron. Mater.* **2012**, *41*, 1851−1857.
(19) Dong, G. H.; Zhu, Y. J.; Chen, L. D. *Cryst. Eng. Commun.* **2011**, *13*, 6811−6816.
(20) Dong, G. H.; Zhu, Y. J.; Chen, L. D. *J. Mater. Chem.* **2010**, *20*, 1976−1981.
(21) Zhang, Y. L.; Mehta, R. J.; Belley, M.; Han, L.; Ramanath, G.; Borca-Tasciuc, T. *Appl. Phys. Lett.* **2012**, *100*, 193113−193113-4.
(22) Antimony telluride (Sb_2Te_3) Debye temperature, heat capacity. In *Springer Materials - The Landolt-Börnstein Database*; Madelung, O., Rössler, U., Schulz, M., Eds.; Springer: New York, 1998; Vol. *41C*; DOI: 10.1007/10681727_1053.
(23) Horak, J.; Lostak, P.; Benes, L. *Philos. Mag. B* **1984**, *50*, 665−671.
(24) Simon, G.; Eichler, W. *Phys. Status Solidi B* **1981**, *107*, 201−206.
(25) Zhang, Y. Thermal and thermoelectric transport in nanostructured materials from pnictogen chalcogenide nanoplate crystals. Ph.D. Dissertation, Rensselaer Polytechnic Institute, Troy, NY, 2012.
(26) Chizhevskaya, S. N.; Shelimova, L. E. *Inorg. Mater.* **1995**, *31*, 1083−1095.
(27) Purkayastha, A.; Kim, S.; Gandhi, D. D.; Ganesan, P. G.; Borca-Tasciuc, T.; Ramanath, G. *Adv. Mater.* **2006**, *18*, 2958−2963.
(28) Carroll, T. X.; De, J.; Maclaren, D. C.; Thomas, T. D.; Saethre, L. J. *J. Electron Spectrosc. Relat. Phenom.* **1987**, *42*, 281−284.
(29) Horak, J.; Cermak, K.; Koudelka, L. *J. Phys. Chem. Solids* **1986**, *47*, 805−809.
(30) Heremans, J. P.; Jovovic, V.; Toberer, E. S.; Saramat, A.; Kurosaki, K.; Charoenphakdee, A.; Yamanaka, S.; Snyder, G. J. *Science* **2008**, *321*, 554−557.
(31) Chasse, T.; Berg, U. *Cryst. Res. Technol.* **1985**, *20*, 1475−1479.
(32) Fang, F.; Opila, R. L.; Venkatasubramanian, R.; Colpitts, T. *J. Vac. Sci. Technol. A* **2011**, 29−35.
(33) Poudel, B.; Hao, Q.; Ma, Y.; Lan, Y. C.; Minnich, A.; Yu, B.; Yan, X.; Wang, D. Z.; Muto, A.; Vashaee, D.; Chen, X. Y.; Liu, J. M.; Dresselhaus, M. S.; Chen, G.; Ren, Z. *Science* **2008**, *320*, 634−638.